

ARTICLE

<https://doi.org/10.1038/s43246-019-0002-9>

OPEN

Active spatial control of terahertz plasmons in graphene

Ngoc Han Tu¹, Katsumasa Yoshioka¹, Satoshi Sasaki¹, Makoto Takamura ¹, Koji Muraki¹ & Norio Kumada ^{1*}

Graphene offers the possibility for actively controlling plasmon confinement and propagation by tailoring its spatial conductivity. However, implementation of this concept has been hampered because it is difficult to control the conductivity pattern without disturbing the electromagnetic environment of graphene plasmons. Here we demonstrate full electrical control of plasmon reflection/transmission in graphene at electronic boundaries induced by a transparent patterned zinc oxide gate, which is designed to minimize the electromagnetic coupling to graphene in the terahertz range. This approach enables plasmons to be confined to desired regions. Our approach might be applied to various types of plasmonic devices, paving the way for implementing a programmable plasmonic circuit.

¹NTT Basic Research Laboratories, NTT Corporation, 3-1 Morinosato-Wakamiya, Atsugi 243-0198, Japan. *email: norio.kumada.rb@hco.ntt.co.jp

Controlling spatial patterns of plasmons constitutes a basis for a variety of applications in the fields of plasmonics, metamaterials, and transformation optics^{1–3}. Of particular interest is the active control of plasmon confinement and propagation because it will enable us to develop programmable plasmonic circuits. A promising strategy achieving it is to tailor the spatial conductivity pattern in graphene⁴. It has been proposed that plasmonic components such as waveguides, splitters, and switches can be developed in a continuous graphene sheet^{4–6}. Using these components in an active manner, a programmable plasmonic circuit can be configured. Experimentally, however, plasmonic response in graphene with a controlled conductivity profile has been poorly explored—most of the intensive works on graphene plasmonics has focused on frequency tuning in a cavity structure with the boundary physically defined by etching^{7–10}, placing metals¹¹, or patterning the substrate¹². While plasmon reflection by an electronic boundary formed at a grain boundary^{13,14}, moiré-patterned graphene interface¹⁵, and monolayer/bilayer interface¹⁶, or one defined by inhomogeneous chemical doping^{17–19} has been observed, these boundaries are unerasable and thus the plasmon reflection cannot be turned off.

To fully control the plasmon reflection/transmission at an electronic boundary, which is essential for the active spatial control of graphene plasmons, independent tuning of the carrier density on both sides of the boundary is necessary. The optical conductivity of graphene depends on the carrier density n (or Fermi energy $E_F \propto \pm \sqrt{|n|}$, with + for electrons and – for holes) as²⁰

$$\sigma = -\frac{ie^2k_B T}{\pi\hbar^2(\omega - i\tau^{-1})} \ln \left[\exp\left(\frac{-E_F}{k_B T}\right) + \exp\left(\frac{E_F}{k_B T}\right) + 2 \right], \quad (1)$$

where e is electron charge, k_B is Boltzmann's constant, ω is angular frequency, τ is scattering time, and T is temperature. Plasmon reflection at a boundary for a step-like σ change is given by²¹

$$R = \frac{|\sigma_1 - \sigma_2|}{|\sigma_1 + \sigma_2|} \approx \frac{||E_{F,1}| - |E_{F,2}||}{||E_{F,1}| + |E_{F,2}||}. \quad (2)$$

This can be varied between zero and unity by tuning the carrier densities $n_{1,2}$. Therefore, by tailoring the carrier density profile across designed boundaries, it is possible, in principle, to construct a plasmonic circuit in a continuous graphene sheet. It is important to note that Eq. (2) holds only when the width of the boundary is much shorter than the plasmon wavelength²¹. When the carrier density varies smoothly, plasmon reflection is suppressed as has been employed for plasmon phase modulator²².

Here we present design principle of device structures for inducing sharp electronic boundaries without disturbing the electromagnetic environment. Using devices fabricated, we demonstrate that plasmon reflectivity can be varied continuously from zero to a large value by adjusting the carrier density difference between adjacent regions. Based on this functionality, we show the ability to confine plasmons into desired regions. The frequency of confined plasmons can also be electrically controlled.

Results

Device design and experiments. To tune the carrier density profile, electrical gates are ineluctable. Moreover, an electronic boundary has to be sharp to prevent the deterioration of the performance of plasmonic devices, and modulation of the electromagnetic environment must be avoided; otherwise, uncontrollable plasmon reflection is inevitable. The first requirement can be satisfied by placing a patterned gate close to graphene as has been employed for controlling reflection of ballistic electrons at DC

regime^{23–25}. However, the nearby gate electrode easily affects the electromagnetic environment, so the selection of the gate material satisfying the second requirement is the key issue at high frequency. To find an appropriate material, we simulated the coupling in the THz range between uniform graphene and a patterned gate for several conductivity values of the gate electrodes (Fig. 1a). When the gate conductivity is high, acoustic plasmons with the electric field confined between graphene and the gate electrode are formed (inset of Fig. 1a)^{26–28}. This induces unwanted plasmon reflection at the gate boundaries, giving rise to absorption peaks in the transmission spectrum. When the conductivity is lower than 10^3 S m^{-1} , on the other hand, the absorption peaks disappear, and the spectrum can be described by the Drude model of free carrier absorption in uniform graphene. In this case, without having uncontrollable boundaries, plasmon reflection can be controlled purely by the carrier density profile.

Based on the simulation, we selected 20-nm-thick zinc oxide (ZnO) with conductivity of $\lesssim 10^3 \text{ S m}^{-1}$ for the gate material. To investigate the basic functionality of plasmon reflection represented by Eq. (2), we patterned the ZnO gate into a simple one-dimensional periodic structure with the width of $2 \mu\text{m}$ spaced by $4 \mu\text{m}$. We used a dual-back-gate structure consisting of the ZnO gate and a p-doped semi-transparent Si substrate (Fig. 1b). Monolayer graphene grown by chemical vapor deposition was transferred onto a 21-nm-thick Al_2O_3 insulating layer deposited on the ZnO gate. The carrier densities of the graphene on the ZnO gate (n_{ZnO}) and on the Si gate (n_{Si}) can be independently tuned by the biases on each gate, V_{ZnO} and V_{Si} . We measured extinction spectra $1 - T(\omega)/T_{\text{ref}}(\omega)$ by Fourier transform infrared spectroscopy with the normally incident radiation polarized perpendicular to the ZnO pattern, where $T_{\text{ref}}(\omega)$ is the transmission power at the charge neutrality point (CNP) used as a reference. All the measurements were conducted at room temperature in the vacuum condition.

Active spatial control of plasmon confinement. Figure 2a, b presents the two-terminal resistance obtained by sweeping V_{ZnO} and V_{Si} , respectively, while keeping the other gate bias fixed at 0 V. The values of n_{ZnO} and n_{Si} (top axis in Fig. 2a, b) can be estimated from $n_{\text{ZnO(Si)}} = C_{\text{ZnO(Si)}}(V_{\text{ZnO(Si)}} - V_{\text{ZnO(Si)}}^{\text{CNP}})/e$, where $C_{\text{ZnO(Si)}}$ is the gate capacitance and $V_{\text{ZnO(Si)}}^{\text{CNP}}$ is the gate bias at the CNP. Using the dielectric constant of 9 and 4 for the Al_2O_3 and SiO_2 insulating layers, respectively, both n_{ZnO} and n_{Si} at $V_{\text{ZnO}} = V_{\text{Si}} = 0 \text{ V}$ are calculated to be $\sim -2.7 \times 10^{12} \text{ cm}^{-2}$, indicating that the graphene is uniformly p-doped at zero gate bias.

Now we know the carrier density profile at each gate bias. To investigate its effects on the plasmon excitations, we measured extinction spectra for several values of $|n_{\text{ZnO}}|$ between 0 and $5.4 \times 10^{12} \text{ cm}^{-2}$ at a fixed $|n_{\text{Si}}| = 2.7 \times 10^{12} \text{ cm}^{-2}$. Figure 2c–e shows the spectra for three representative density profiles. When the carrier density is uniform ($n_{\text{ZnO}} = n_{\text{Si}}$) (Fig. 2d), the extinction increases monotonically with decreasing frequency, as well-described by the Drude model. This verifies that, as simulated, the presence of the ZnO gate does not induce plasmon reflection. Note also that the structural step of $\sim 15 \text{ nm}$ at the boundaries (Supplementary Note 1) does not induce the reflection. When the carrier density modulation is introduced, the incoming light can resonantly excite plasmons with the wavelength determined by the modulation profile. One extreme case is that graphene on the ZnO gate is set to the CNP ($n_{\text{ZnO}} \sim 0$). In this case, a single peak appears at 2.3 THz (Fig. 2e). This peak can be assigned to the plasmon mode confined in the $4\text{-}\mu\text{m}$ -wide graphene regions on the Si gate. Actually, the peak frequency corresponds to the plasmon frequency of 2.3 THz in a graphene micro-ribbon cavity

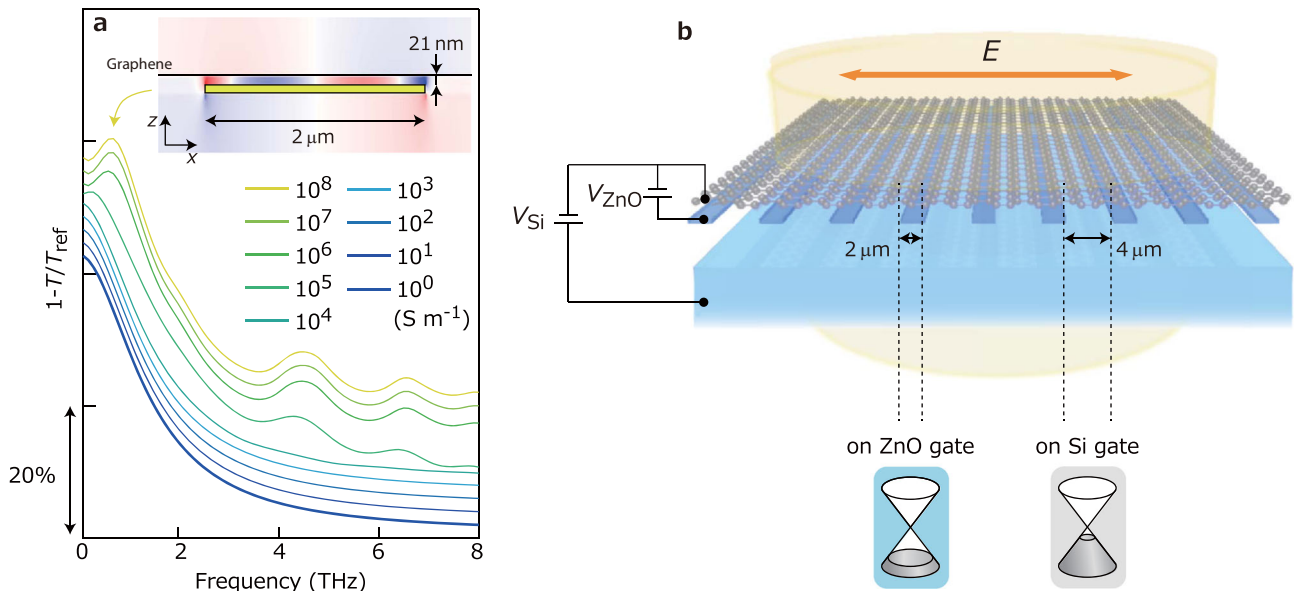


Fig. 1 Device structure. **a** Simulated transmission spectra for several values of the patterned-gate conductivity. The thickness of the gate was set at 20 nm, two orders of magnitude smaller than the plasmon wavelength in the THz range, to minimize the dielectric modulation. Traces are vertically offset by 2%. Inset shows the simulated plasmon field E_z (expanded to the z direction) at 0.7 THz for the patterned-gate conductivity of 10^8 S m^{-1} . The yellow box represents a patterned gate. The conductivity of a typical metal and the ZnO used is $\sim 10^8$ and $\lesssim 10^3 \text{ S m}^{-1}$, respectively. **b** Schematic representation of the device employing a dual-back-gate structure. The 20-nm-thick ZnO film is patterned into a one-dimensional periodic structure with the width of $2 \mu\text{m}$ spaced by $4 \mu\text{m}$ on the Si/SiO₂ substrate. The patterned ZnO ribbons are connected at both ends to apply the gate bias. The transferred graphene and the ZnO gate are separated by a 21-nm-thick Al₂O₃ insulating layer. By adjusting gate biases V_{ZnO} and V_{Si} , the carrier densities of graphene on the ZnO gate and on the Si gate can be independently tuned. Polarization of the THz light is perpendicular to the carrier density modulation pattern.

fabricated by etching⁹ with the width $W = 4 \mu\text{m}$,

$$\omega_p = \sqrt{\frac{e^2 v_F \sqrt{\pi} |n|}{2\epsilon^* \epsilon_0 \hbar W}}, \quad (3)$$

where $\epsilon^* = 4$ is the dielectric constant. When $|n_{\text{ZnO}}|$ is twice as large as $|n_{\text{Si}}|$, two resonance peaks appear (Fig. 2c). The additional peak at 4.7 THz originates from plasmons confined in the 2- μm -wide graphene regions on the ZnO gate. The overall increase in the extinction with decreasing frequency is due to the remnant free carrier absorption, indicating the presence of finite transmission across the boundaries. These results indicate that plasmon reflection can be introduced electrically by the carrier density modulation in continuous graphene.

Next we show the ability to actively control plasmonic cavities in real space. By tuning V_{ZnO} and V_{Si} , uniform conditions ($n_{\text{ZnO}} = n_{\text{Si}}$) at different carrier densities can be obtained (Fig. 3a). Then, by setting one of the gates to the CNP, plasmon cavities are formed. The frequency of the cavity mode (Fig. 3b, c) depends on the width of the active regions ($W = 2$ or $4 \mu\text{m}$) and increases with $|n|^{1/4}$ as expected from Eq. (3) (Fig. 3d). This demonstrates that the spatial position and frequency of a plasmon cavity can be controlled electrically. Real-time switching of plasmon active/inactive regions can be applied for programmable waveguides and switches not limited to cavities. Note that deviation of the peak frequency from Eq. (3) is discernible for smaller n_{ZnO} at $n_{\text{Si}} \sim 0$ (blue circles in Fig. 3d). This can be explained by the existence of plasmons supported by thermally excited electrons and holes at the CNP²⁶ in graphene on the Si gate (Supplementary Note 2). Note also that some additional peaks for higher frequency are artifacts, not higher order modes, whose frequency should change systematically with the carrier density (Supplementary Fig. 2).

Continuous tuning of plasmon reflectivity. To extend our device structure to other plasmonic components such as tunable

beam splitters and modulators, continuous tuning of the reflection coefficient is necessary. To show how the reflection coefficient evolves with the carrier density profile, we decompose the measured spectra into the free carrier absorption and plasmon resonance contributions by fitting the spectra with the superposition of the Drude function and two Lorentzian functions (Fig. 4a):

$$\sigma(\omega) = \alpha \frac{i}{\omega + i\omega\tau_D^{-1}} + \beta \frac{\omega}{\omega^2 - \omega_{p1}^2 + i\omega\tau_{p1}^{-1}} + \gamma \frac{\omega}{\omega^2 - \omega_{p2}^2 + i\omega\tau_{p2}^{-1}}, \quad (4)$$

where α , β , and γ are coefficients. Then, as the measure of the plasmon reflection coefficient, we calculated the area ratio $A_r = A_{\text{Lor}} / (A_{\text{Lor}} + A_{\text{Drude}})$, where A_{Lor} and A_{Drude} are the spectral areas of the Lorentzian and Drude components (pink and sky blue areas in Fig. 4a), respectively ($A_r = 0$ and 1 for the perfect transmission and full reflection, respectively). Figure 4b shows A_r for different density profiles, $0 \leq |n_{\text{ZnO}}| \leq 5.4 \times 10^{12} \text{ cm}^{-2}$ and $|n_{\text{Si}}| = 2.7 \times 10^{12} \text{ cm}^{-2}$. As discussed above, when the carrier density is uniform ($|n_{\text{ZnO}}| = |n_{\text{Si}}|$), the spectrum can be described only by the Drude component, which gives $A_r = 0$. As $|n_{\text{ZnO}}|$ deviates from $|n_{\text{Si}}|$, A_r increases gradually and reaches a maximum of 0.54 at $|n_{\text{ZnO}}| \sim 0$. This behavior can be reproduced by R in Eq. (2) (solid line in Fig. 4b). Equation (2) suggests that the non-perfect reflection at $|n_{\text{ZnO}}| \sim 0$ is mostly due to the finite temperature effect (Supplementary Note 3). The agreement between the experimental results and the simple model indicates that the reflection coefficient is determined purely by the carrier density profile.

Discussion

Finally, we discuss the evolution of the resonance frequencies. Figure 4c, d compiles the spectra for $0 \leq |n_{\text{ZnO}}| \leq 5.4 \times 10^{12} \text{ cm}^{-2}$ and $|n_{\text{Si}}| = 2.7 \times 10^{12} \text{ cm}^{-2}$ and their Lorentzian component (the full set of the spectra are presented in Supplementary Fig. 4). As

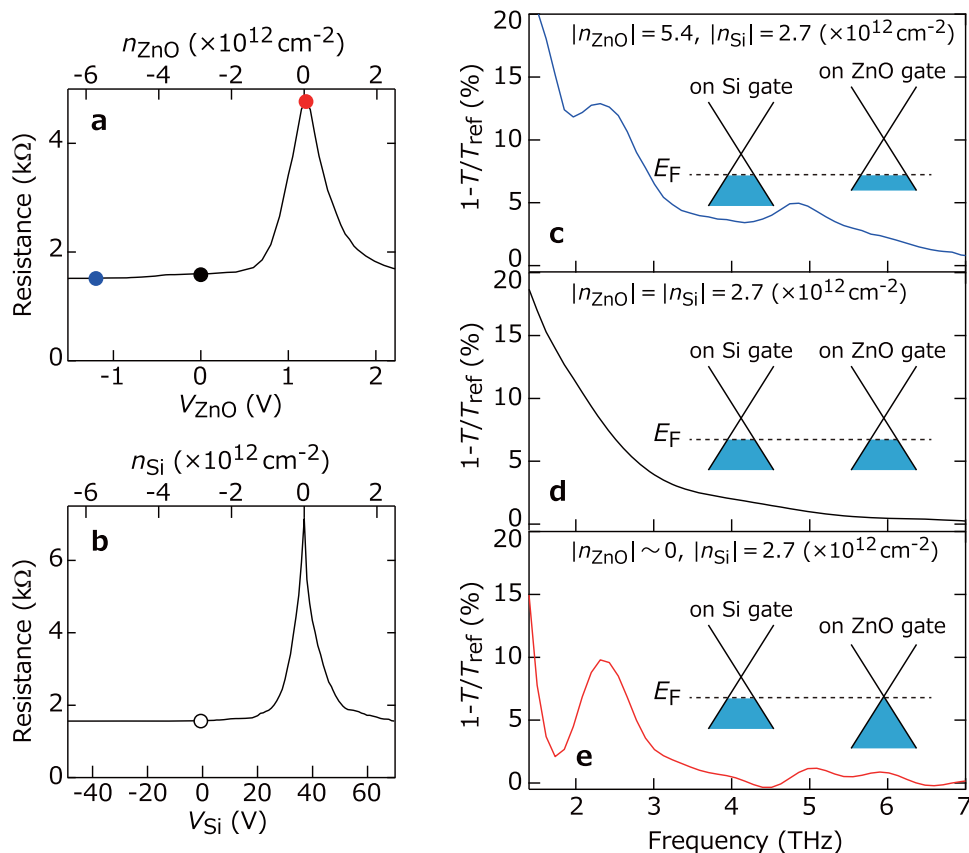


Fig. 2 Extinction spectra for representative carrier density profiles. **a, b** Two-terminal resistance obtained by sweeping V_{ZnO} (V_{Si}) while keeping $V_{\text{Si}} = 0$ V ($V_{\text{ZnO}} = 0$ V). The current direction is parallel to the ZnO pattern. Carrier density in each region calculated from the gate capacitance and the distance to the CNP is indicated on the top axes. **c–e** Extinction spectra $1 - T/T_{\text{ref}}$ for three representative carrier density profiles: **c** $|n_{\text{ZnO}}| > |n_{\text{Si}}| > 0$, **d** $|n_{\text{ZnO}}| = |n_{\text{Si}}| > 0$, and **e** $|n_{\text{ZnO}}| \sim 0$, $|n_{\text{Si}}| > 0$. Solid circles in **(a)** and the open circle in **(b)** represent the gate conditions used for **(c–e)**.

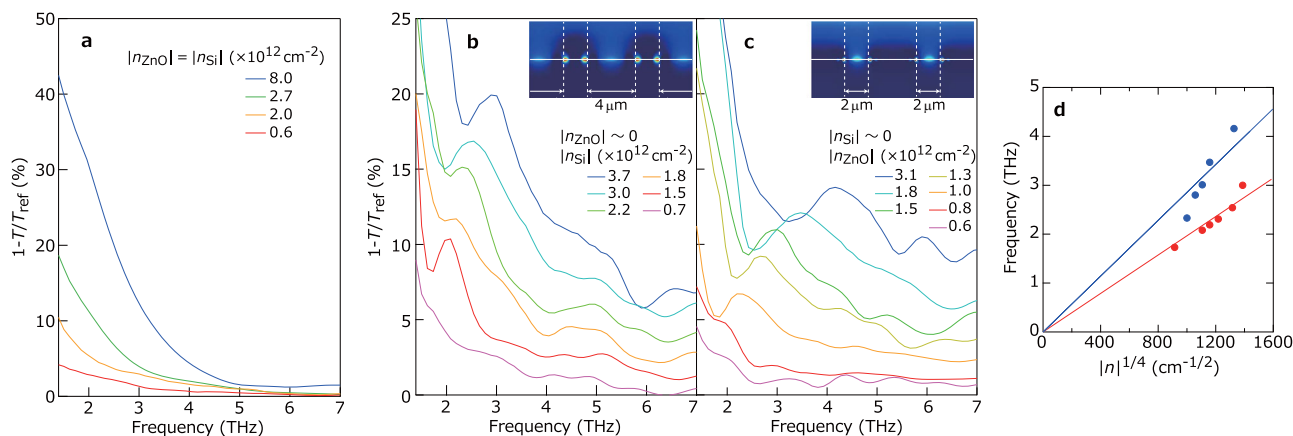


Fig. 3 Selective activation of plasmonic cavity. **a** Extinction spectra for uniform conditions ($|n_{\text{ZnO}}| = |n_{\text{Si}}|$) at several values of carrier density. **b, c** Extinction spectra for $|n_{\text{ZnO}}| \sim 0$ ($|n_{\text{Si}}| \sim 0$) for several values of $|n_{\text{Si}}|$ ($|n_{\text{ZnO}}|$). Each trace is vertically offset by 1%. The insets show the simulated electric field intensity at resonance frequencies for the carrier density of $3.0 \times 10^{12} \text{ cm}^{-2}$ in the plasmon active regions. The horizontal solid and vertical dotted lines indicate the position of the graphene and boundaries, respectively. **d** Plasmon resonance frequency obtained from the spectra in **b** (red circles) and **c** (blue circles) as a function of $|n|^{1/4}$. Red and blue lines represent calculated plasmon frequency in cavities with $W = 4$ and $2 \mu\text{m}$, respectively, based on Eq. (3).

shown by the peak frequencies as a function of $|n_{\text{ZnO}}|$ (Fig. 4d), when $|n_{\text{ZnO}}| \gtrsim 3.5 \times 10^{12} \text{ cm}^{-2}$, the spectra show two resonance peaks consistent with the two cavity modes with $W = 2$ and $4 \mu\text{m}$ (red and blue lines in Fig. 4e). Two resonance peaks also appear for $|n_{\text{ZnO}}| \lesssim 1.8 \times 10^{12} \text{ cm}^{-2}$. Although the frequency of the two independent cavity modes coincides at $|n_{\text{ZnO}}| = 0.6 \times 10^{12} \text{ cm}^{-2}$,

the observed peak frequencies show anti-crossing behavior, indicating the presence of capacitive coupling between the two cavity modes. Between the two regions, where $|n_{\text{ZnO}}| \sim |n_{\text{Si}}|$, the reflection coefficient is not large enough to confine plasmons. In such a regime, the THz radiation can couple plasmons with the wavelength corresponding to the modulation period ($\lambda = 6 \mu\text{m}$). The

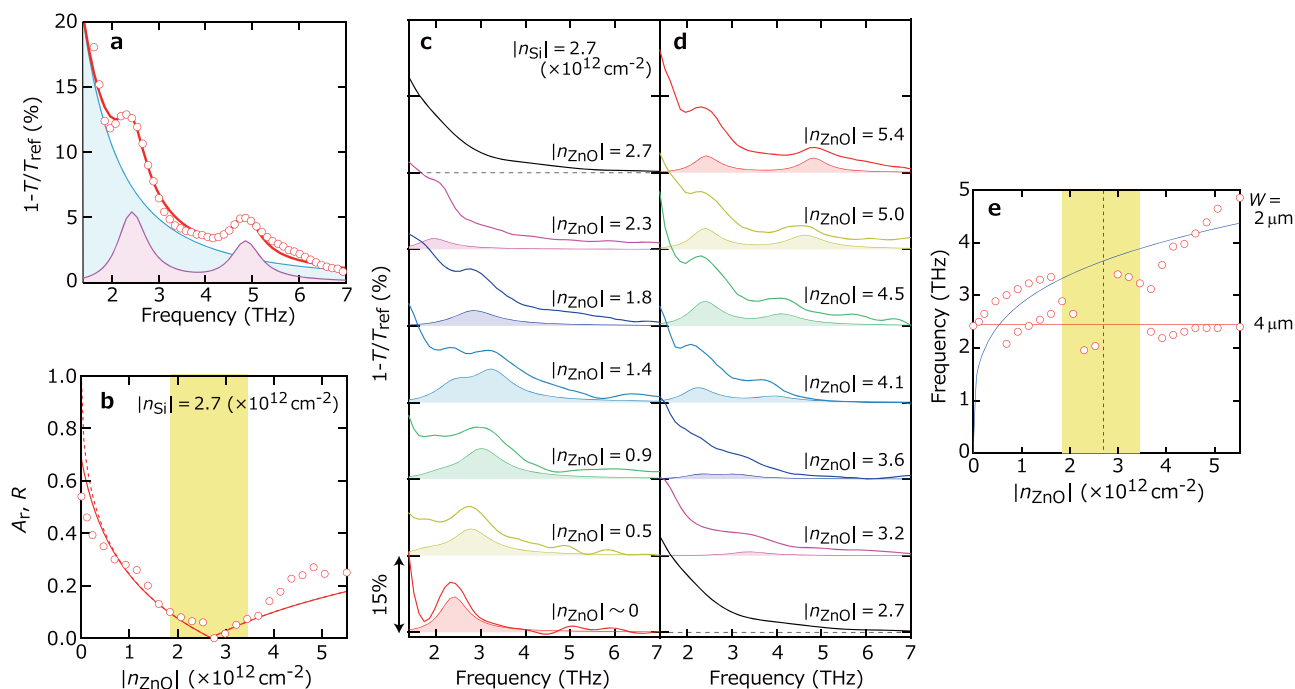


Fig. 4 Evolution of reflection coefficient and resonance frequency. **a** Spectrum for $|n_{\text{ZnO}}| = 5.4$ and $|n_{\text{Si}}| = 2.7 \times 10^{12} \text{ cm}^{-2}$ with fitting line based on Eq. (4). Sky blue and pink areas (A_{Dru} and A_{Lor}) represent the Drude and Lorentzian components, respectively. **b** Area ratio $A_r = A_{\text{Lor}} / (A_{\text{Lor}} + A_{\text{Dru}})$ (open circles) as a function of $|n_{\text{ZnO}}|$ for fixed $|n_{\text{Si}}| = 2.7 \times 10^{12} \text{ cm}^{-2}$. The solid and dashed lines are the reflection coefficient R obtained from Eq. (2) with $T = 300$ and 0 K , respectively. **c, d** Spectra (solid lines) and Lorentzian components (solid areas), where (**c**), (**d**) compile the data for $0 \leq |n_{\text{ZnO}}| \leq |n_{\text{Si}}|$ and $|n_{\text{Si}}| \leq |n_{\text{ZnO}}| \leq 5.4 \times 10^{12} \text{ cm}^{-2}$, respectively. Traces are vertically offset by 15%. **e** Summary of the resonance frequency as a function of $|n_{\text{ZnO}}|$. Red and blue lines are the frequency of the cavity modes [Eq. (3)] with $W = 4$ and $2 \mu\text{m}$, respectively. The vertical dashed line indicates $|n_{\text{ZnO}}| = |n_{\text{Si}}|$.

frequency of this mode is expected to be in the middle between the two cavity modes with $\lambda/2 = 2$ and $4 \mu\text{m}$. This model is consistent with the observation of single peaks but not sufficient to fully explain the peak frequencies around $|n_{\text{ZnO}}| = 2.7 \times 10^{12} \text{ cm}^{-2}$. Supper-lattice effects²⁹ should be involved in this weak reflection regime. Further experiments at lower temperature to obtain sharper resonance peaks would provide a better understanding of the behavior of the resonance frequencies.

In conclusion, we controlled plasmonic response in a continuous graphene sheet by modulating the spatial profile of the carrier density. We demonstrated that position, size, and frequency of plasmon cavities can be controlled electrically. We also showed continuous variation of the plasmon reflection coefficient at a boundary for a step-like change in the carrier density. These functionalities can be applied to a variety of plasmonic applications, not limited to cavities. As it is possible to make the ZnO/Al₂O₃ gate multilayer on top and bottom of a graphene sheet, a complex carrier density pattern can be formed. Therefore, our device structure can be a platform for implementing a programmable plasmonic circuit.

Methods

Device fabrication. We used Si/SiO₂ substrate with SiO₂ thickness of 285 nm. Weakly doped Si served as a back gate. A 20-nm-thick ZnO layer was formed on SiO₂ by atomic layer deposition (ALD). We measured the THz transmission of the ZnO film and found that it was about 90% in the whole experimental range (Supplementary Fig. 5). After patterning the ZnO layer by photolithography, a 21-nm-thick Al₂O₃ layer was formed on the patterned substrate by another ALD process. Finally, a large sheet of monolayer graphene grown by chemical vapor deposition on a copper foil was wet-transferred onto the top. Typical sample size is $5 \times 5 \text{ mm}^2$. Two ohmic contacts were deposited outside the illumination region.

Electromagnetic simulation of graphene plasmon. A two-dimensional finite element calculation was performed using commercially available software (COMSOL) to investigate the influence of the gate electrode on the plasmonic response of

the continuous graphene. We calculated THz extinction spectra of our device structure, including the Al₂O₃ insulating layer and Si/SiO₂ substrate, for several values of the patterned-gate conductivity. The graphene was modeled as a uniform conducting sheet based on the Kubo formula [Eq. (1)] with $E_F = 0.25 \text{ eV}$, $\tau = 1 \text{ ps}$, and $T = 300 \text{ K}$. The conductivity of the patterned gate was simulated by using the Drude model given by $\sigma = \sigma_{\text{DC}} / (1 - i\omega/\Gamma_{\text{gate}})$, where σ_{DC} is the DC conductivity and Γ_{gate} is the scattering rate of the gate. The result obtained using the highest conductivity of 10^8 S m^{-1} in Fig. 1b corresponds to the value of the metallic gate (e.g., the DC conductivity of gold is $\sim 4 \times 10^7 \text{ S m}^{-1}$). On the other hand, the DC conductivity of our ZnO gate is $\sim 1 \text{ S m}^{-1}$, which is the lowest simulated conductivity in Fig. 1b. We used $\Gamma_{\text{gate}} = 50 \text{ THz}$ for every simulation, which is reasonable for the ZnO gate³⁰.

Data availability

The data that support the findings of this study are available from the corresponding authors upon request.

Received: 17 September 2019; Accepted: 13 November 2019;

Published online: 04 February 2020

References

- Barnes, W. L., Dereux, A. & Ebbesen, W. Surface plasmon subwavelength optics. *Nature* **424**, 824–830 (2003).
- Chen, H., Chan, C. T. & Sheng, P. Transformation optics and metamaterials. *Nat. Mater.* **9**, 387–396 (2010).
- Zentgraf, T., Liu, Y., Mikkelsen, M. H., Valentine, J. & Zhang, X. Plasmonic lense and Eaton lenses. *Nat. Nanotechnol.* **6**, 151–155 (2011).
- Vakil, A. & Engheta, N. Transformation optics using graphene. *Science* **332**, 1291–1294 (2011).
- Shi, B. et al. Tunable band-stop filters for graphene plasmons based on periodically modulated graphene. *Sci. Rep.* **6**, 26796 (2016).
- Gómez-Díaz, J. S. & Perruisseau-Carrier, J. Graphene-based plasmonic switches at near infrared frequencies. *Opt. Express* **21**, 15490–15504 (2013).
- Ju, L. et al. Graphene plasmonics for tunable terahertz metamaterials. *Nat. Nanotechnol.* **6**, 630–643 (2011).
- Yan, H. et al. Tunable infrared plasmonic devices using graphene/insulator stacks. *Nat. Nanotechnol.* **7**, 330–334 (2012).

9. Yan, H. et al. Infrared spectroscopy of tunable dirac terahertz magneto-plasmons in graphene. *Nano. Lett.* **12**, 3766–3771 (2012).
10. Poumirol, J.-M. et al. Electrically controlled terahertz magneto-optical phenomena in continuous and patterned graphene. *Nat. Commun.* **8**, 14626 (2016).
11. Jadidi, M. M. et al. Tunable terahertz hybrid metal-graphene plasmons. *Nano. Lett.* **15**, 7099–7104 (2015).
12. Gao, W. et al. Excitation and active control of propagating surface plasmon polaritons in graphene. *Nano. Lett.* **13**, 3698–3702 (2013).
13. Fei, Z. et al. Electronic and plasmonic phenomena at graphene grain boundaries. *Nat. Nanotechnol.* **8**, 821–825 (2013).
14. Gerber, J. A., Berweger, S., O’Callahan, B. T. & Raschke, M. B. Phase-resolved surface plasmon interferometry of graphene. *Phys. Rev. Lett.* **113**, 055502 (2014).
15. Ni, G. X. et al. Plasmons in graphene moiré superlattices. *Nat. Mater.* **14**, 1217–1222 (2015).
16. Alonso-González, P. et al. Controlling graphene plasmons with resonant metal antennas and spatial conductivity patterns. *Science* **344**, 1369–1373 (2014).
17. Wang, D. et al. Quantum control of graphene plasmon excitation and propagation at heaviside potential steps. *Nano. Lett.* **18**, 1373–1378 (2018).
18. Tu, N. H., Takamura, M., Ogawa, Y., Suzuki, S. & Kumada, N. Plasmon confinement by carrier density modulation in graphene. *Jpn. J. Appl. Phys.* **57**, 110307 (2018).
19. Takamura, M., Kumada, N., Wang, S., Kumakura, K. & Taniyasu, Y. Plasmon control driven by spatial carrier density modulation in graphene. *ACS Photon.* **6**, 947–952 (2019).
20. Hanson, W. G. Dyadic Green’s functions and guided surface waves for a surface conductivity model of graphene. *J. Appl. Phys.* **103**, 064302 (2008).
21. Rosolen, G. & Maes, B. Nonuniform doping of graphene for plasmon tapers. *J. Opt.* **17**, 015002 (2015).
22. Woessner, A. et al. Electrical 2π phase control of infrared light in a 350-nm footprint using graphene plasmons. *Nat. Photon.* **11**, 421–424 (2017).
23. Williams, J. R., Low, T., Lundstrom, M. S. & Marcus, C. M. Gate-controlled guiding of electrons in graphene. *Nat. Nanotechnol.* **6**, 222–225 (2011).
24. Rickhaus, P. et al. Ballistic interferences in suspended graphene. *Nat. Commun.* **4**, 2342 (2013).
25. Rickhaus, P. et al. Guiding of electrons in a few-mode ballistic graphene channel. *Nano. Lett.* **15**, 5819–5825 (2015).
26. Alonso-González, P. et al. Acoustic terahertz graphene plasmons revealed by photocurrent nanoscopy. *Nat. Nanotechnol.* **12**, 31–35 (2017).
27. Iranzo, D. A. et al. Probing the ultimate plasmon confinement limits with a van der Waals heterostructure. *Science* **360**, 291–295 (2018).
28. Lee, I.-H., Yoo, D., Avouris, P., Low, T. & Oh, S.-H. Graphene acoustic plasmon resonator for ultrasensitive infrared spectroscopy. *Nat. Nanotechnol.* **14**, 313–320 (2019).
29. Machens, U., Heitmann, D., Prager, L., Kotthaus, J. P. & Beinvogl, W. Minigaps in the plasmon dispersion of a two-dimensional electron gas with spatially modulated charge density. *Phys. Rev. Lett.* **53**, 1485–1488 (1984).
30. Ma, G. et al. Carrier concentration dependence of terahertz transmission on conducting ZnO films. *Appl. Phys. Lett.* **93**, 211101 (2008).

Acknowledgements

We thank M. Hashisaka and H. Irie for fruitful discussions, M. Ono for valuable help, and A. Tsukada for experimental support.

Author contributions

N.-H.T. fabricated samples and performed all experiments, analyzed data, and wrote the paper. K.Y. performed the simulation and discussed the results. S.S. fabricated samples and evaluated the ZnO properties. M.T. grew graphene. K.M. discussed the results. N.K. planned the experiments, discussed the results, and wrote the paper. All the authors commented on the paper.

Competing interests

The authors declare no competing interests.

Additional information

Supplementary information is available for this paper at <https://doi.org/10.1038/s43246-019-0002-9>.

Correspondence and requests for materials should be addressed to N.K.

Reprints and permission information is available at <http://www.nature.com/reprints>

Publisher’s note Springer Nature remains neutral with regard to jurisdictional claims in published maps and institutional affiliations.

 **Open Access** This article is licensed under a Creative Commons Attribution 4.0 International License, which permits use, sharing, adaptation, distribution and reproduction in any medium or format, as long as you give appropriate credit to the original author(s) and the source, provide a link to the Creative Commons license, and indicate if changes were made. The images or other third party material in this article are included in the article’s Creative Commons license, unless indicated otherwise in a credit line to the material. If material is not included in the article’s Creative Commons license and your intended use is not permitted by statutory regulation or exceeds the permitted use, you will need to obtain permission directly from the copyright holder. To view a copy of this license, visit <http://creativecommons.org/licenses/by/4.0/>.

© The Author(s) 2020